



1 **Impacts of Long-range Transport of Aerosols on Marine Boundary Layer Clouds in**
2 **the Eastern North Atlantic**

3 **Yuan Wang^{1,2,*}, Xiaojian Zheng³, Xiquan Dong³, Baike Xi³, Peng Wu³, Timothy Logan⁴,**
4 **Yuk L. Yung^{1,2}**

5 ¹Division of Geological and Planetary Sciences, California Institute of Technology, Pasadena,
6 CA, USA

7 ²Jet Propulsion Laboratory, California Institute of Technology, Pasadena, CA, USA

8 ³Department of Hydrology and Atmospheric Sciences, University of Arizona, Tucson, AZ, USA

9 ⁴Department of Atmospheric Sciences, Texas A&M University, College Station, TX, USA

10

11 *Corresponding author: Yuan Wang (yuan.wang@caltech.edu)



12 **Abstract**

13 Vertical profiles of aerosols are inadequately observed and poorly represented in climate models,
14 contributing to the current large uncertainty associated with aerosol-cloud interactions. The DOE
15 ARM Aerosol and Cloud Experiments in the Eastern North Atlantic (ACE-ENA) aircraft field
16 campaign near the Azores islands provided ample accurate observations of vertical distributions
17 of aerosol and cloud properties. Here we utilize the in situ aircraft measurements from the ACE-
18 ENA and ground-based remote sensing data along with an aerosol-aware Weather Research and
19 Forecast (WRF) model to characterize the aerosols due to long-range transport over a remote
20 region and to assess their possible influence on marine boundary-layer (MBL) clouds. The vertical
21 profiles of aerosol and cloud properties measured via aircraft during the ACE-ENA campaign
22 provide detailed information revealing the physical contact between transported aerosols and MBL
23 clouds. The ECMWF-CAMS aerosol reanalysis data can reproduce the key features of aerosol
24 vertical profiles in the remote region. The cloud-resolving WRF sensitivity experiments with
25 distinctive aerosol profiles suggest that the transported aerosols and MBL cloud interactions (ACI)
26 require not only low-altitude aerosol preferably getting close to the marine boundary layer top, but
27 also large cloud top height variations. Based on those criteria, the observations show the
28 occurrence of ACI involving the transport of aerosol over the Eastern North Atlantic is about 62%
29 in summer. For the case with noticeable long-range transport aerosol effect on MBL cloud, the
30 susceptibilities of droplet effective radius and liquid water content are -0.11 and $+0.14$,
31 respectively. When varying on the similar magnitude, aerosols originating from the boundary layer
32 exert larger microphysical influence on MBL clouds than those entrained from free troposphere.



33 **1. Motivation and Background**

34 It has been long hypothesized that increased high concentrations of aerosols serving as
35 cloud condensation nuclei (CCN) can reduce cloud droplet effective radius, enhance cloud albedo,
36 suppress drizzle formation, and change cloud lifetime and fraction, the so-called aerosol indirect
37 effects (AIE) (Twomey, 1977; Seinfeld et al., 2016). However, current radiative forcing stemming
38 from cloud responses to anthropogenic aerosols remains highly uncertain in the climate system,
39 representing the largest challenge in climate predictions (Fan et al., 2016). Note that the current
40 IPCC assessment mainly considers the warm stratus and stratocumulus response to aerosols
41 (Myhre et al., IPCC, 2013), while aerosol induced convective cloud response (Wang et al., 2014)
42 as well as with anthropogenic aerosol effect as ice nuclei (Zhao et al., 2019) have not been fully
43 accounted for yet. Even for warm clouds, the climate significance of whether liquid water content
44 and cloud lifetime are enhanced or reduced by CCN is still widely debated (Malavelle et al., 2017;
45 Toll et al., 2019; Rosenfeld et al., 2019). Due to the nonlinear nature of cloud responses to CCN
46 perturbations, the largest cloud susceptibility and AIE typically occurs for marine boundary layer
47 (MBL) clouds over remote regions (Garrett and Hobbs, 1995; Carslaw et al., 2014; Dong et al.,
48 2015). Under the pristine conditions with extremely low background CCN concentration
49 (Kristensen et al., 2016), any aerosol intrusion following long-range transport has great potential
50 to alter the local aerosol/CCN budget (Roberts et al., 2006). Hence, in this study, we aim to
51 characterize long-range transport of aerosols and to assess their impacts on MBL clouds by
52 combining in situ aircraft measurements with cloud-resolving model simulations.

53 For those aerosols resulting from long-range transport, one of the most important aspects
54 pertinent to aerosol-cloud interactions (ACI) is their vertical distribution, or in other words, their
55 position relative to cloud layers. The vertical distribution of aerosols can be affected by a number
56 of complex atmospheric processes, such as emission, transport, deposition, as well as
57 microphysical and chemical processes. Previous studies suggest that aerosols can alter MBL cloud
58 microphysical properties and enhance indirect effects through entrainment into the cloud top when
59 either aerosol particles settle or the cloud deck deepens (Painemal et al., 2014, Lu et al., 2018). In
60 the boundary layer of remote regions like the equatorial Pacific, the majority of CCN were found
61 to be supplied by long-range transport instead of local emission or formation (Clarke et al., 2013).
62 Recent aircraft observations from the NASA's Ob-seRvations of Aerosols above CLouds and their
63 intEractionS (ORACLES) campaign showed distinctive MBL cloud responses to aerosols above



64 and below cloud depending on the history of smoke entrainment (Diamond et al., 2018). Therefore,
65 it is critical to understand aerosol variability as a function of height and its influence on the aerosol
66 indirect forcing assessment over the regions where MBL clouds are abundant.

67 Spaceborne active sensors that possess vertically profiling capability have been widely
68 used to characterize aerosol and cloud spatial variations and to detect the aerosol above clouds
69 (Painemal et al., 2014; Jiang et al., 2018). However, satellites likely miss the thin aerosol layers
70 with relatively low concentration (but still higher than maritime background values), and thus
71 overestimate the distance between the aerosol plume base and the cloud top using the spaceborne
72 observations. Therefore, aircraft observations with continuous vertical sampling are the most
73 reliable source that can accurately characterize the vertical relationship between aerosol and cloud.
74 The DOE ARM Aerosol and Cloud Experiments in the Eastern North Atlantic (ACE-ENA) aircraft
75 field campaign near the Azores islands provided a unique opportunity to study aerosols from
76 different sources and their impacts on MBL clouds (Wang et al., 2019). The ENA site is located
77 in the remote northeastern Atlantic Ocean where MBL clouds are prevalent throughout the year
78 due to the warm sea surface temperature and prevailing subsidence near the edge of the Hadley
79 cell (Wood et al., 2015, Dong et al. 2014). The site also receives complex air mass dictated by
80 different wind patterns. In addition to the local maritime air, the airflows originating from either
81 the North American or the Saharan region complicate the local aerosol types and sources (Logan
82 et al., 2014). This study leverages the airborne measurements of aerosol vertical profiles for
83 different chemical species to understand aerosols and their influence on MBL cloud microphysical
84 properties over the Azores, with the ultimate goal to provide observational constraints on the global
85 climate model simulations. An aerosol reanalysis product is evaluated in the present study as well.

86 Even with aircraft measured vertical relationship between aerosol and cloud, it is difficult
87 to estimate whether the aerosol aloft can impact the cloud beneath, as the microphysical processes
88 such as entrainment into cloud top cannot be directly measured. Hence, we employ aerosol-aware
89 cloud-resolving simulations to simulate the MBL cloud development and aerosol transport in the
90 free troposphere and to quantify the AIE. Through the sensitivity experiment by imposing different
91 aerosol vertical profiles, we can disentangle aerosol and other confounding meteorological factors
92 in ACI, which is challenging to do using only short-term observations. Section 2 describes the
93 main observational data and introduces the numerical modeling tools. Section 3 reports the
94 observed aerosols and clouds based on aircraft measurements and reanalysis product. Section 4



95 presents the analyses of cloud-resolving simulations using the WRF model. Section 5 summarizes
96 the key finding in this study and provide additional discussions for the study's caveats and future
97 work.

98 **2. Methodology**

99 **2.1 Aircraft Observations and Ancillary Data Descriptions**

100 Vertical distributions of aerosols and MBL cloud microphysical properties over the Azores
101 were obtained during ACE-ENA two intensive operational periods (IOPs), i.e. early summer 2017
102 (late June to July) and winter 2018 (January to February). Since the aerosol concentration and
103 variability are much larger in the summertime of Azores, we will mainly focus on the 2017 July
104 in this study. The ARM Aerial Facility (AAF) Gulfstream-159 (G-1) provides accurate
105 measurements of aerosol size distribution, total aerosol number concentration, and chemical
106 constituents below and above cloud layers during the summer IOP. The Condensation Particle
107 Counter (CPC) on board the G1 can detect aerosol particles larger than 10 nm, and it can provide
108 profiles of condensation nuclei number concentration (N_{CN}) when the aircraft ascends or descends.
109 Note that N_{CN} measurements inside cloud can be contaminated and thus have large uncertainty.
110 Cloud condensation nuclei (CCN) number concentration (N_{CCN}) is obtained by the CCN-200
111 particle counter on board the G1 aircraft. The N_{CCN} is measurement under the controlled
112 supersaturation of 0.35% with the humidified particle size range from 0.75 μm to 10 μm (Rose et
113 al., 2008). We analyze sulfate and organic carbon (OC) mass concentrations measured by the
114 Aerodyne high-resolution time of flight aerosol mass spectrometer (HR-ToF-AMS) and refractory
115 black carbon (BC) from the Single Particle Soot Photometer (SP2).

116 We use cloud and drizzle microphysical property profiles retrieved from a combination of
117 ground-based observations including a Ka-band ARM Zenith Radar, ceilometer, and microwave
118 radiometer. Fast Cloud Droplet Probe (Glienke and Mei, 2020) measured cloud droplet properties
119 (diameter between 1.5 and 46 μm), and 2-Dimensional Stereo Prob (2DS, Glienke and Mei, 2019)
120 measured drizzle properties (diameter greater than 45 μm) were used to evaluate the ground-based
121 retrievals. Following Dong et al. (1997) and Frisch et al. (1995, 1998), cloud droplet size
122 distribution was assumed as a lognormal distribution. Differently, drizzle size distribution was
123 assumed as a normalized Gamma distribution, as suggested by O'Connor et al. (2005) and Ulbrich
124 (1983). The retrieved cloud and drizzle properties are validated against collocated aircraft in situ
125 measurements during ACE-ENA (Wu et al., 2020). Both the time series and vertical profiles from



126 the retrievals agree well with in situ observations. Treating the aircraft measurements as cloud
127 truth, the median retrieval uncertainties are estimated as ~20% for cloud droplet effective radius,
128 ~30% for cloud droplet number concentration, liquid water content (LWC) and drizzle drop
129 median radius.

130 To characterize long-range aerosol intrusions over the monthly time scale, we employ
131 global aerosol reanalysis data, namely the Copernicus Atmosphere Monitoring Service (CAMS).
132 It provides four-dimensional mass concentrations of aerosols and reactive gases with a horizontal
133 spatial resolution of approximately 80 km and 60 vertical levels. The CAMS reanalysis was
134 constructed by assimilating several satellite products of the atmospheric constituents into a global
135 model and data assimilation system (Flemming et al., 2017). The assimilated satellite datasets
136 include aerosol optical depth (AOD) from MODIS and AATSR, CO from MOPITT, NO₂ and O₃
137 from OMI, GOMES, etc.

138 **2.2 Model Description**

139 The Weather Research and Forecasting (WRF) model version 3.6 is employed in this study
140 to simulate MBL clouds and their possible interactions with transported aerosols. Four nested
141 domains are setup with horizontal resolutions of 19.2 km, 4.8 km, 1.2 km, and 300 m (SI Fig. 1).
142 Even for the innermost domain, we try to cover as large area as possible, considering the highly
143 heterogeneous meteorological conditions in the mid-latitudes. The innermost domain is configured
144 in a similar way with large-eddy simulations and it uses the 3-dimensional Smagorinsky first order
145 closure for eddy coefficient computation. Boundary layer parameterization is turned off for this
146 domain. Note that 300-m horizontal resolution does not strictly meet the classic LES requirement,
147 but recent simulations with similar resolutions successfully reproduced the structure and drizzle
148 onset of MBL clouds (Wang and Feingold, 2009) and were used to study boundary layer cloud
149 interactions with aerosols (Lin et al., 2016). The 65 stretched sigma levels are used with a 40 m
150 vertical resolution within MBL. The large-scale forcing is adopted from the ERA5 reanalysis data
151 with 25 km horizontal resolution (Copernicus Climate Change Service, 2017).

152 To accurately depict MBL cloud microphysical processes, a spectral bin microphysical
153 (SBM) scheme is employed which utilizes a pair of 33 bins to represent cloud/rain drops and
154 aerosols separately without prescribed size distributions (Fan et al., 2012; Wang et al., 2013).
155 Aerosol activation is explicitly calculated using the model predicted water vapor supersaturation.
156 The Köhler theory is used to calculate the critical radius. The hygroscopicity of sulfate is assumed



157 for aerosols in each size bin. At each timestep, aerosols with radius greater than the critical radius
158 are removed from the aerosol spectrum and the mass of the activated droplets is added to the cloud
159 spectrum. Aerosol regeneration from complete evaporation of droplets and/or raindrops is also
160 considered in SBM. Since the aerosol size distribution in SBM ranges from a few nanometers to a
161 few microns, the definition of aerosol in the model is closer to the condensation nuclei in the
162 aircraft observation. Hence, observed vertical profiles of N_{CN} from selected cases are used for the
163 initial and lateral boundary conditions of aerosols in the model. The model integrates from 1200
164 UTC on the day before the selected case, and the first 12 hours is considered as spin-up. Shortwave
165 and longwave radiation transfer calculations are accounted for by the Goddard and RRTM schemes,
166 respectively. The radiative effect of aerosols above the cloud decks is not considered in the present
167 model setup. We speculate such an effect is small, because of rather low aerosol optical depth over
168 this remote region, even with the long-range transported aerosols (aside from thick dust plumes
169 from the Saharan Desert).

170 **3. Observational Data Analysis**

171 **3.1 Characterization of aerosol vertical distribution using the CAMS reanalysis**

172 Previous study showed that the CAMS aerosol product exhibit good agreement with
173 ground-based observations such as AERONET and unassimilated satellite products such as MISR
174 on the global scale (Christophe et al., 2019). The global spatial correlation of CAMS AOD with
175 AERONET is about 0.83, and the bias in CAMS AOD seasonal variation is between -10% and
176 +20%. Here we utilize this dataset to characterize the aerosol vertical distribution over the
177 northeast Atlantic during the ACE-ENA field campaign. Vertical distributions and their temporal
178 evolutions for five types of aerosols, including sulfate, organic carbon (OC), black carbon (BC),
179 sea salt, and dust, over the whole month of July 2017 are displayed in Fig. 1 based on the CAMS
180 aerosol reanalysis. Sulfate, OC, and BC are the predominant aerosol types possibly possessing an
181 anthropogenic signature. BC and OC can also originate from biomass burning. Those aerosols
182 share a similar spatiotemporal pattern in the free troposphere, indicating that they undergo similar
183 long-range transport before arriving over the Azores island. Marked and persistent low-altitude (1-
184 2 km) pollution transport occurred between 1-13 July, as shown in the evolution of vertical profiles
185 of sulfate, OC and, BC (Figs. 1a-1c). High-altitude (3-6 km) pollution transport occurred between
186 6-20 July for those three aerosol types as well. Both modes of pollution transport occurred 50% of
187 the time during July 2017, indicating a high frequency of long-range transport over this area. July



188 18 and 12 presents the typical high- and low- plume cases, respectively, so they will be investigated
189 thoroughly in the later aircraft data analyses and model simulations. The concentrations of OC,
190 BC, and sulfate are generally low in the MBL, so aerosol penetration from the free troposphere
191 into the lower MBL may be not significant during this month. One exception is sulfate during 18-
192 21 July. Sulfate concentration experienced an increase in the MBL followed by a lag increase in
193 the free troposphere. Since there is no significant transport signal before and during that time
194 period, the elevated sulfate concentration within the boundary layer is due likely to some local
195 sources such as oxidation of marine dimethyl sulfate (DMS).

196 The aerosols of natural sources, namely sea salt and dust, show different vertical
197 distributions (Figs. 1d -1e). Sea salt aerosols mainly reside near the surface and are rarely found
198 above 1000 m. Dust particles are mainly found at high altitudes, typically above 3 km, during 5-
199 14 July, indicating their long-range transport. However, the dust spatiotemporal pattern in the free
200 troposphere are quite distinctive from sulfate and smoke, implying the different sources of long-
201 range transport. Previous studies suggest the possible dust transport from the Saharan Desert to
202 the northeast Atlantic region (Logan et al., 2014; Weinzierl et al., 2015). To address those issues,
203 back-trajectory analyses were conducted, and the results will be discussed later. During 15-19 July,
204 dust particles are found within the boundary layer and even near the surface following the presence
205 of dust plume in the free troposphere earlier. Such a downward propagation does not occur for
206 anthropogenic aerosols either, likely explained by the fact that dust particles are bigger in size with
207 larger settling velocity.

208 **3.2 Identification of source regions using back-trajectory analysis**

209 The backward ensemble trajectories were computed using the NOAA Hybrid Single-
210 Particle Lagrangian Integrated Trajectory (HYSPPLIT) (Stein et al., 2015) model, based on the
211 large-scale meteorological fields from Global Data Assimilation System (GDAS) with a spatial
212 resolution of 0.5°. We focus on three cases/days to examine the sources of typical high- and low-
213 altitude plumes of anthropogenic aerosols and mineral dust. The model uses an end-point height
214 of 1.5, 2.4, and 3 km for three selected cases to represent the air parcels in the anthropogenic low-
215 altitude, high-altitude, and dust plumes, respectively. To capture the different lengths of transport
216 procedure, the model was backward integrated for 7 days for the anthropogenic aerosols and 13
217 days for the mineral dust case. 20 ensemble members are employed for each case. They agree with
218 each other better on horizontal trajectory than vertical displacement. Larger differences are found



219 among the ensemble members after three days for anthropogenic aerosols and after two days for
220 dust.

221 The back-trajectory analyses confirm that the source region of sulfate, BC, and OC in the
222 plumes is the North American continent (Fig. 2a,c), consistent with previous analyses of data from
223 the earlier field campaign over the ENA site (Logan et al., 2014). The westerly jet carries the
224 pollutants across the Atlantic Ocean, and it takes three to four days to arrive the Azores. Temporal
225 evolutions of trajectory vertical displacement reveal when aerosols are elevated from the PBL to
226 the free troposphere and such information can be used to pinpoint the aerosol source. Fig. 2b,d
227 suggests that aerosols are mainly from the central US in the high-plume case, and from eastern US
228 in the low-plume case. The curved trajectories in the low-plume case reflect the influence of the
229 Bermuda/Azores High located to the south. The dust transports exhibit a much different pathway.
230 Starting at 3km altitude, the back-trajectory develops westward initially, but sharply turn around
231 and point to the North Africa (Fig. 2e,f). It suggests that Sahara is the most likely source for the
232 dust particles observed over the Azores.

233 Note that back-trajectory analysis of air mass has its own limitations. For example,
234 shipping emissions over Northern Atlantic Ocean are not considered in the present analysis. Also,
235 the source attribution based on episodic events may be not representative for the climatological
236 mean scenario. Therefore, the source attribution results here need to be further evaluated in future
237 studies which can utilize more sophisticated approach such as source tagging in the GCM nudged
238 by the reanalysis data (Wang et al., 2014).

239 **3.3 Vertical distributions of different aerosols in aircraft observations**

240 Aircraft observations during the ACE-ENA provide more accurate depictions of aerosol
241 vertical distribution and aerosol layer heights relative to cloud layer heights, with differentiation
242 of aerosols type and hygroscopicity. During the summer IOP, quite diverse aerosol vertical profiles
243 are found. Here we focus on those with noticeable aerosol plumes in the free troposphere. Fig. 3
244 shows two representative vertical distributions of aerosol mass concentrations averaged over the
245 flights on July 18 and 12, corresponding to the high- and low-altitude aerosol plume, respectively.
246 In the high-altitude plume case, BC, OC, and sulfate concentrations all increase with height above
247 clouds, indicating downward propagation of aerosol plumes and possible interaction with MBL
248 clouds. BC and OC concentrations are even higher than that of sulfate in the free troposphere,
249 suggesting the biomass burning signature of the plume on that day. Conversely, within MBL, much



250 higher concentration of sulfate in the MBL than those of BC and OC. This phenomenon is also
251 captured by the CAMS aerosol reanalysis (Fig. 1a), lending support to the fidelity of the reanalysis
252 dataset. For the low altitude plume (Fig. 3b), the vertical gradients of aerosol concentrations are
253 not clear above clouds, but aerosol concentrations within 500 m right above clouds are higher than
254 those near the cloud base (Fig. 3b), corroborating the physical contact between aerosol plumes and
255 MBL clouds. Comparing Fig. 3 and 1, the CAMS reanalysis data generally agree with aircraft
256 observed aerosol profiles on the selected days, but the predicted aerosol mass mixing ratios are an
257 order of magnitude higher in the reanalysis data. Those discrepancies point out that any
258 quantitative usage of aerosol reanalysis product should be cautious.

259 Aerosol and CCN concentration vertical profiles are also available from the aircraft
260 observations. For the high-altitude plume, N_{CN} reaches a peak of $\sim 600 \text{ cm}^{-3}$ at 2.5 km, and then
261 decreases dramatically downwards to $\sim 180 \text{ cm}^{-3}$ near cloud top ($\sim 1.1 \text{ km}$), which is even lower
262 than N_{CN} values within the boundary layer ranging from 200 to 300 cm^{-3} on that day (Figure 4a).
263 The measured 200-m average of N_{CN} above cloud top is 185 cm^{-3} , smaller than that below cloud
264 base 290 cm^{-3} (Table 1). From the surface to the 2.5 km height, the minimum N_{CN} occurs near
265 cloud top, reflecting the disconnection between MBL aerosols and those from long-range transport
266 aloft. The characteristics of N_{CCN} profile are similar with those of N_{CN} . In the low-altitude plume,
267 both N_{CN} and N_{CCN} show a slower decline of above the cloud layer (Fig. 4c,d). Also, the right-
268 above-cloud-top N_{CN} and N_{CCN} at 1 km are higher than those below the cloud layer, indicating the
269 physical contact of the aerosol plume with the cloud deck.

270 During the summer IOP, the aircraft was deployed in twenty days to collect data. Among
271 those days, only eight of them have stable MBL clouds during the flight hours, according to the
272 ground-based cloud radar. We summarize the aircraft observed aerosol and cloud vertical
273 distribution characterizations for those eight days/cases in Table 1. Among those eight cases, five
274 days show an increase in above-cloud N_{CN} along with height, and one day shows roughly constant
275 N_{CN} above clouds, all of which indicate the existence of long-range transport of aerosols in the
276 free troposphere and downward propagating influence on the aerosol budget near the cloud top.
277 Moreover, five out of eight cases have above-cloud N_{CN} (within 200 m) significantly larger than
278 below cloud N_{CN} , implying the potential influence of free-troposphere aerosols on MBL clouds
279 from another angle of view.

280 **4. WRF modeling of MBL clouds and their response to transported aerosols**



281 In observation of quite diverse aerosol vertical profiles in the real atmosphere, an
282 outstanding science question is under what conditions the long-range transported aerosols can
283 exert significant impacts on the MBL clouds beneath. To answer this question and to quantify the
284 related aerosol indirect effects, cloud-resolving WRF simulations are performed, focusing on the
285 two selected cases with the high- and low-altitude plume on 18 July and 11 July, respectively. In
286 the model control simulations, the aircraft measured aerosol profiles are used to set up initial and
287 lateral boundary conditions of aerosol total number concentration for the two cases (Fig. 5).
288 Sensitivity simulations for clean scenarios are conducted by replacing the observed aerosol
289 concentrations above cloud with an assumed exponential decrease of N_{CN} along with height in the
290 free troposphere instead. Before sensitivity analyses, we want to examine to what extent the cloud-
291 resolving simulations can reproduce the local-scale meteorological variations and MBL cloud
292 structure at Azores. Here we use the high-altitude plume case as an example to evaluate the
293 model's fidelity in the northeast Atlantic.

294 The large-scale wind pattern and boundary layer structure from the model control run are
295 compared against the interpolated soundings over the ARM ENA site. Fig. 6 shows that the model
296 exhibits good agreement with the observed air temperature, moisture content, and relative
297 humidity. The model captures the cold/dry air advection at 1 km height in the morning followed
298 by the warm/moist air in the afternoon. The persistent supersaturation between 500 and 1000 m
299 and associated cloud deck are also reproduced in the simulation. We find that the key model
300 configuration to reproduce the main features of meteorological variability is to have appropriate
301 domain nesting and dynamical downscaling. Particularly, the outmost domain with 19.2 km grid
302 spacing is crucial and necessary for this mid-latitude region. The region is featured by frequent
303 mesoscale weather systems, and local wind and moisture fields vary drastically even within a day.
304 The model setup with only three domains of 4.8 km, 1.2 km, and 300 m horizontal resolution
305 induce large errors in the vertical profiles of moisture and temperature. A persistent dry bias occurs
306 near the MBL top when the outmost domain with 19.2 km grid spacing is absent. Such
307 meteorological biases further influence cloud simulation and result in discontinuous cloud layer in
308 its temporal evolution.

309 MBL cloud properties simulated by WRF are evaluated against the retrievals from a
310 combination of ground-based observations. The simulation captures the cloud top height at 1 km
311 and cloud bottom height at 500 m during the day (Fig. 7a,b). Therefore, the cloud physical



312 thickness is comparable between model and observation. LWC is generally smaller in the model
313 than that in the observation. Meanwhile, the simulation captures the larger LWC near the top of
314 the cloud, reflecting the adiabatic growth of cloud droplet starting from the cloud bottom. The
315 temporal evolution of simulated LWCs does not match well with retrievals, partly due to the spatial
316 sampling bias. Cloud droplet effective radius (R_e) in the model is calculated as a function of
317 volume-mean droplet radius as well as relative dispersion (a ratio between standard deviation and
318 mean radius in a size distribution) (Liu and Daum, 2002). The model shows the comparable
319 vertical distribution of R_e with cloud radar retrievals, e.g. the larger R_e near the cloud top, but with
320 larger variability in the size range than observations (Fig. 7c,d).

321 To explore the sensitivity of MBL cloud microphysical properties to the long-range aerosol
322 transport, we contrast the simulations with and without observed long-range aerosol plumes in the
323 free troposphere. For the high-altitude plume (July 18) case, the comparisons of model run with
324 different aerosol vertical profiles show that both LWC and cloud fraction remain largely
325 unchanged, whether the aerosol plume above 1.5 km exists or not. In fact, the cloud top height on
326 that day experienced some temporal variations near the Azores, as it extended to 1.5 km during
327 the night due to strong radiative cooling and reduced to 1 km during the most of daytime. As a
328 result, the distance between the aerosol plume and cloud deck varied from 500 m to less than 100
329 m. Fig. 8a-f show that the long-range transported aerosols have no significant impacts on the MBL
330 cloud properties underneath when the physical distance between aerosol plume and cloud layer is
331 greater than 100 m. This finding does not support the previous study based on satellite products
332 arguing that aerosol-cloud interactions are still discernable with aerosol plumes 1 km above the
333 cloud deck (Painemal et al. 2014).

334 To answer the question at what height aerosol plume starts to influence MBL cloud
335 microphysical properties, we perform an additional simulation by lowering the aerosol plume
336 bottom from 1.5 km to 1.1 km which is considered as the height of MBL and cloud tops during
337 the daytime. In this sensitivity run, the aerosol indirect effect remains largely muted during the
338 daytime. It suggests that when boundary layers and cloud decks are relatively stable, long-range
339 transport aerosols have a low chance of being entrained into the cloud top and being activated to
340 cloud droplets. However, when the cloud deck becomes deeper at night, particularly after 2200
341 UTC when a significant part of the cloud extends into the aerosol layer above 1.1 km, an increase
342 in LWC by up to 0.1 g m^{-3} is observed (Fig. 8g-h).



343 In contrast, the simulated clouds in the low-altitude plume (July 12) case exhibit large
344 variations in the vertical (Fig. 9), and consequently the aerosol plume just above the cloud top
345 imposes significant influence on the MBL cloud micro- and macro-physical properties. The mean
346 LWC is increased by 5.7%, and cloud fraction is increased by 5.4%, due to a 48.0% increase in
347 CCN under the influence of the long-range aerosol transport. The distinctive responses of MBL
348 clouds to aerosol plumes at different heights reinforce the notion that the vertical overlap between
349 aerosol and cloud layers is crucial for ACI pertinent to the long-range aerosol transport. Moreover,
350 the extent of overlap is jointly controlled by aerosol plume height and cloud top variation. The
351 latter is particularly important, when the boundary layer is relatively stable, and the aerosol vertical
352 mixing is rather weak for most marine stratus.

353 It is a nontrivial task to identify the physical contact between an aerosol plume and a cloud
354 deck based on the aircraft measurements. Especially when the center of an aerosol plume is
355 hundreds of meters above cloud top and aerosol concentration right above the cloud is lower than
356 that within PBL, it is difficult to estimate whether aerosols can be entrained into the cloud layer.
357 As the above model results suggested, ACI requires critical mass of aerosols immersed into the
358 cloud layers. Here we define a “critical altitude” at which above-cloud N_{CN} is equal to the below-
359 cloud N_{CN} . With such a concept, we can compare this altitude to the cloud top variation during a
360 period of interest. Take the July 18 case for example, according to the airborne measurements, the
361 critical altitude is 1674 m, well beyond the range of cloud top variation (880 – 1300 m) on that
362 day (Table 1). Thus, we can reach a conclusion that, even though long transport of aerosols was
363 found in the free troposphere on that day, they were unlikely to interfere with MBL clouds below.
364 Here we take all the airborne measured vertical information into account, including aerosol
365 changes above clouds, comparison of above- and below-cloud N_{CN} , as well as cloud top height
366 variations, and We revisit the eight observed cases in Table 1. We find that five days (0628, 0630,
367 0706, 0712, and 0715) out of eight during the summer phase of the ACE-ENA field campaign
368 clearly show the interactions between aerosols from long-range transport and local MBL clouds,
369 corresponding to a 62.5% occurrence frequency.

370 The previous cloud-resolving modeling studies of aerosol effects on MBL cloud properties
371 either used a constant CCN concentration throughout the whole domain (Yamaguchi et al., 2019)
372 or the CCN profiles in MBL were prescribed with an exponential decrease in the free troposphere
373 (Wang et al., 2013, 2018; Lin et al., 2016). The consequent sensitivity experiments were conducted



374 by perturbing CCN at different heights with the same scaling factor, without differentiating the
375 aerosols from different sources. Therefore, those studies share a common assumption that the
376 CCNs are solely from a local source impacted by local boundary layer processes. Here we repeat
377 this type of CCN perturbation experiment and compare the resultant aerosol effects with our
378 current assessment for the effects of long-rang transported aerosols only. Three idealized CCN
379 profiles are used for the July 18 cases. The cloud susceptibility (ratio between logarithmic cloud
380 property change and logarithmic CCN change) derived from the comparison of those three
381 idealized runs are found to range from -0.22 to -0.25 for R_e and from $+0.18$ to $+0.30$ for LWC
382 (Fig. 10a-b). Both R_e and LWC susceptibility values are close to the high ends of the most of
383 current AIE assessments (Sato and Suzuki, 2018; Zheng et al., 2020). For the noticeable long-
384 range transport effect in the July 12 case, the R_e and LWC susceptibilities are -0.11 and $+0.14$,
385 respectively. They are smaller than those from the idealized MBL aerosol perturbation experiments.
386 Hence, this suggests that the aerosols of long-range transport are less efficient in altering MBL
387 cloud properties than those originating from local sources. It can be attributed to the fact that dry
388 air likely enters cloud layer along with CCN, resulting in less supersaturation and reduced
389 activation rate.

390 5. Conclusion and Discussion

391 Located in the remote eastern North Atlantic, the Azores islands experience frequent long-
392 range transport of smoke and anthropogenic aerosols from continental U.S. A recent DOE ARM
393 ACE-ENA aircraft field campaign near the Azores in the summer of 2017 provides ample
394 observations of aerosols and clouds with detailed vertical information. In this study, we combine
395 the aircraft measurements, CAMS aerosol reanalysis, and an aerosol-aware and cloud-resolving
396 WRF model to characterize spatial variations of aerosols from long-range transport over the
397 Azores islands and assess their possible influence on the marine boundary layer clouds. The
398 reanalysis data show high frequency of occurrence of long-range transport over this area.
399 Evaluated by airborne aerosol measurement, the CAMS reanalysis data generally reproduce
400 observed aerosol profiles over this remote region, but the predicted aerosol mass mixing ratios are
401 still significantly biased. Our back-trajectory analyses confirm that anthropogenic and/or biomass
402 burning aerosols were mainly from the U.S. continent during the summer phase of ACE-ENA,
403 while the dust plumes are mainly originated from Sahara.

404 Aircraft observations show distinctive aerosol vertical distribution scenarios when long-



405 range transport of aerosols is noticeable. In some cases, a sharp decrease in aerosol concentration
406 downwards the cloud top with a minimal value right above the cloud top, while in other cases,
407 moderate decrease with a higher aerosol concentration near the cloud top than below the cloud
408 bottom. To identify the requirement for the long-range transported aerosols to exert significant
409 impacts on the MBL clouds beneath, a series of cloud resolving WRF simulations are conducted
410 for the selected cases. The model with dynamical downscaling from 19 km horizontal resolution
411 down to 300 m grid spacing is found reliable in simulating the vertical variability of temperature
412 and humidity fields over the Azores island, as well as in capturing the basic cloud structure. By
413 imposing aerosol plumes at the observed heights and varying them in the sensitivity runs, the
414 simulation results suggest the aerosol plume cannot affect underlying MBL cloud properties when
415 the center of the plume is over 100 m higher than cloud top. Even when the aerosols are right on
416 top of the stratified MBL cloud deck, the deepening of cloud and destabilization of boundary layer
417 are required to have significant aerosol-cloud interactions. We find more marine cloud fractions
418 with larger water content by the aerosols from long-range transport when the aerosol layer is
419 emerged into the cloud deck. For the case with noticeable long-range transport aerosol effect on
420 MBL cloud, the susceptibilities of droplet effective radius and liquid water content are -0.11 and
421 $+0.14$, respectively. Additional model sensitivity experiments are conducted, which perturb the
422 whole-column aerosol concentration without changing the shape of their vertical profiles. The
423 results show much larger susceptibility of cloud effective radius and liquid water path to the similar
424 magnitude of aerosol perturbation in PBL, indicating that the long-range transported aerosols are
425 less efficient in altering MBL cloud properties than those originated from local sources.

426 Through the comparisons of above- and below-cloud aerosol concentrations and the
427 examination of aerosol plume and cloud top height variations, we find about 63% occurrence
428 frequency of the interaction between remote aerosol and local MBL cloud based on the eight flights
429 during the summer phase of the ACE-ENA field campaign. Such a high frequency indicates the
430 importance of long-range transport aerosols on MBL clouds. Note that, due to the limited sample
431 size, the frequency may not be accurate to represent the true value on the daily basis. To our
432 knowledge, our study represents the first effort to utilize the ACE-ENA aircraft campaign data to
433 study the impacts of long-range transported aerosols on MBL clouds. Future study will focus on
434 the comparison of AIE involving long-range transport aerosols between different ARM sites and
435 field campaigns.



436

437

438 **Code availability**

439 The code of WRF model used in this study is available at
440 <https://www2.mmm.ucar.edu/wrf/users/downloads.html>.

441

442 **Data availability**

443 All the WRF model simulation output used for this research can be downloaded from the website
444 at <http://web.gps.caltech.edu/~yzw/share/Wang-2020-ACP-Azores>. The aircraft and ground-
445 based measurements used in this study were obtained from the Atmospheric Radiation
446 Measurement (ARM) Program sponsored by the U.S. Department of Energy (DOE) Office of
447 Energy Research, Office of Health and Environmental Research, and Environmental Sciences
448 Division. The data can be downloaded from <http://www.archive.arm.gov/>. CAMS global aerosol
449 reanalysis product at pressure level used in this study can be downloaded at
450 <https://apps.ecmwf.int/datasets/data/cams-nrealtime/levtype=pl/>. ERA5 data is available for
451 download via the Copernicus Climate Data Store website (<https://cds.climate.copernicus.eu>).

452

453 **Acknowledgement**

454 This study was primarily supported by the collaborative NSF grant (Award No. AGS-1700727,
455 1700728). We acknowledge helpful discussions on the model setup with Dr. Zheng Lu at Texas
456 A&M University. We thank the instrument mentors of the AMS, SP2, and CPC instruments and
457 the individuals collecting measurements during the ACE-ENA field campaign. We also
458 acknowledge high-performance computing support from Pleiades provided at NASA Ames. All
459 requests for materials in this paper should be addressed to Yuan Wang (yuan.wang@caltech.edu).



460 **References**

461

462 Christophe, Y., Schulz, M., Bennouna, Y., Eskes, H.J., Basart, S., Benedictow, A., Blechschmidt,
463 A.-M., Chabrillat, S., Clark, H., Cuevas, E., Flentje, H., Hansen, K.M., Im, U., Kapsomenakis,
464 J., Langerock, B., Petersen, K., Richter, A., Sudarchikova, N., Thouret, V., Wagner, A., Wang,
465 Y., Warneke, T. and Zerefos, C.: Validation report of the CAMS global Reanalysis of aerosols
466 and reactive gases, years 2003-2018, Copernicus Atmosphere Monitoring Service (CAMS)
467 report, CAMS84_2018SC1_D5.1.1-2018_v1.pdf, doi:10.24380/dqws-kg08, 2019

468 Clarke, A. D., Freitag, S., Simpson, R. M. C., Hudson, J. G., Howell, S. G., Brekhovskikh, V. L.,
469 Campos, T., Kapustin, V. N. and Zhou, J.: Free troposphere as a major source of CCN for the
470 equatorial pacific boundary layer: Long-range transport and teleconnections, *Atmos. Chem.*
471 *Phys.*, doi:10.5194/acp-13-7511-2013, 2013.

472 Copernicus Climate Change Service (C3S): ERA5: Fifth generation of ECMWF atmospheric
473 reanalyses of the global climate. Copernicus Climate Change Service Climate Data Store
474 (CDS), available at <https://cds.climate.copernicus.eu/cdsapp> (last access:), 2017.

475 Diamond, M. S., Dobracki, A., Freitag, S., Griswold, J. D. S., Heikkila, A., Howell, S. G., Kacarab,
476 M. E., Podolske, J. R., Saide, P. E. and Wood, R.: Time-dependent entrainment of smoke
477 presents an observational challenge for assessing aerosol-cloud interactions over the
478 southeast Atlantic Ocean, *Atmos. Chem. Phys.*, doi:10.5194/acp-18-14623-2018, 2018.

479 Dong, X., Ackerman, T. P., Clothiaux, E. E., Pilewskie, P. and Han, Y.: Microphysical and
480 radiative properties of boundary layer stratiform clouds deduced from ground-based
481 measurements, *J. Geophys. Res. Atmos.*, doi:10.1029/97jd02119, 1997.

482 Dong, X., Ackerman, T. P. and Clothiaux, E. E.: Parameterizations of the microphysical and
483 shortwave radiative properties of boundary layer stratus from ground-based measurements, *J.*
484 *Geophys. Res. Atmos.*, doi:10.1029/1998JD200047, 1998.

485 Dong, X., Schwantes, A. C., Xi, B. and Wu, P.: Investigation of the marine boundary layer cloud
486 and CCN properties under coupled and decoupled conditions over the azores, *J. Geophys.*
487 *Res.*, doi:10.1002/2014JD022939, 2015.

488 Fan, J., Leung, L. R., Li, Z., Morrison, H., Chen, H., Zhou, Y., Qian, Y. and Wang, Y.: Aerosol
489 impacts on clouds and precipitation in eastern China: Results from bin and bulk microphysics,
490 *J. Geophys. Res. Atmos.*, doi:10.1029/2011JD016537, 2012.



- 491 Fan, J., Wang, Y., Rosenfeld, D. and Liu, X.: Review of aerosol-cloud interactions: Mechanisms,
492 significance, and challenges, *J. Atmos. Sci.*, doi:10.1175/JAS-D-16-0037.1, 2016.
- 493 Flemming, J., Benedetti, A., Inness, A., Engelen J, R., Jones, L., Huijnen, V., Remy, S., Parrington,
494 M., Suttie, M., Bozzo, A., Peuch, V. H., Akritidis, D. and Katragkou, E.: The CAMS interim
495 Reanalysis of Carbon Monoxide, Ozone and Aerosol for 2003-2015, *Atmos. Chem. Phys.*,
496 doi:10.5194/acp-17-1945-2017, 2017.
- 497 Frisch, A. S., Uttal, T., Fairall, C. W. and Snider, J. B.: On the measurement of stratus cloud
498 properties with a cloud radar and microwave radiometer, in *International Geoscience and*
499 *Remote Sensing Symposium (IGARSS)*., 1997.
- 500 Frisch, A. S., Feingold, G., Fairall, C. W., Uttal, T., and Snider, J. B.: On cloud radar and
501 microwave radiometer measurements of stratus cloud liquid water profiles, *J. Geophys. Res.*
502 *Atmos.*, doi:10.1029/98JD01827, 1998.
- 503 Garrett, T. J. and Hobbs, P. V.: Long-range transport of continental aerosols over the Atlantic
504 Ocean and their effects on cloud structures, *J. Atmos. Sci.*, doi:10.1175/1520-
505 0469(1995)052<2977:LRTOCA>2.0.CO;2, 1995.
- 506 Glienke, S. and Mei, F.: Two-Dimensional Stereo (2D-S) Probe Instrument Handbook, DOE ARM
507 Climate Research Facility, DOE/SC-ARM-TR-233, available at
508 https://www.arm.gov/publications/tech_reports/handbooks/doe-sc-arm-tr-233.pdf, 2019.
- 509 Glienke, S., & Mei, F. (2020). Fast Cloud Droplet Probe (FCDP) Instrument Handbook, DOE
510 ARM Climate Research Facility, DOE/SC-ARM-TR-238, available at
511 https://www.arm.gov/publications/tech_reports/handbooks/doe-sc-arm-tr-238.pdf, 2020.
- 512 Jiang, J. H., Su, H., Huang, L., Wang, Y., Massie, S., Zhao, B., Omar, A. and Wang, Z.:
513 Contrasting effects on deep convective clouds by different types of aerosols, *Nat. Commun.*,
514 doi:10.1038/s41467-018-06280-4, 2018.
- 515 Kristensen, T. B., Müller, T., Kandler, K., Benker, N., Hartmann, M., Prospero, J. M.,
516 Wiedensohler, A. and Stratmann, F.: Properties of cloud condensation nuclei (CCN) in the
517 trade wind marine boundary layer of the western North Atlantic, *Atmos. Chem. Phys.*,
518 doi:10.5194/acp-16-2675-2016, 2016.
- 519 Lin, Y., Wang, Y., Pan, B., Hu, J., Liu, Y. and Zhang, R.: Distinct impacts of aerosols on an
520 evolving continental cloud complex during the RACORO field campaign, *J. Atmos. Sci.*,
521 doi:10.1175/JAS-D-15-0361.1, 2016.



- 522 Liu, Y. G., and Daum, P.H.: Anthropogenic aerosols - Indirect warming effect from dispersion
523 forcing. *Nature*, 419, 580-581, 10.1038/419580a, 2002.
- 524 Logan, T., Xi, B. and Dong, X.: Aerosol properties and their influences on marine boundary layer
525 cloud condensation nuclei at the ARM mobile facility over the Azores, *J. Geophys. Res.*,
526 doi:10.1002/2013JD021288, 2014.
- 527 Lu, Z., Liu, X., Zhang, Z., Zhao, C., Meyer, K., Rajapakse, C., Wu, C., Yang, Z. and Penner, J.
528 E.: Biomass smoke from southern Africa can significantly enhance the brightness of
529 stratocumulus over the southeastern Atlantic Ocean, *Proc. Natl. Acad. Sci. U. S. A.*,
530 doi:10.1073/pnas.1713703115, 2018.
- 531 Malavelle, F. F., Haywood, J. M., Jones, A., Gettelman, A., Clarisse, L., Bauduin, S., Allan, R. P.,
532 Karset, I. H. H., Kristjánsson, J. E., Oreopoulos, L., Cho, N., Lee, D., Bellouin, N., Boucher,
533 O., Grosvenor, D. P., Carslaw, K. S., Dhomse, S., Mann, G. W., Schmidt, A., Coe, H., Hartley,
534 M. E., Dalvi, M., Hill, A. A., Johnson, B. T., Johnson, C. E., Knight, J. R., O'Connor, F. M.,
535 Stier, P., Myhre, G., Platnick, S., Stephens, G. L., Takahashi, H. and Thordarson, T.: Strong
536 constraints on aerosol-cloud interactions from volcanic eruptions, *Nature*,
537 doi:10.1038/nature22974, 2017.
- 538 O'Connor, E. J., Hogan, R. J. and Illingworth, A. J.: Retrieving stratocumulus drizzle parameters
539 using doppler radar and lidar, *J. Appl. Meteorol.*, doi:10.1175/JAM-2181.1, 2005.
- 540 Painemal, D., Kato, S. and Minnis, P.: Boundary layer regulation in the southeast Atlantic cloud
541 microphysics during the biomass burning season as seen by the A-train satellite constellation,
542 *J. Geophys. Res.*, doi:10.1002/2014JD022182, 2014.
- 543 Rémillard, J., Kollias, P. and Szyrmer, W.: Radar-radiometer retrievals of cloud number
544 concentration and dispersion parameter in nondrizzling marine stratocumulus, *Atmos. Meas.*
545 *Tech.*, doi:10.5194/amt-6-1817-2013, 2013.
- 546 Roberts, G., Mauger, G., Hadley, O. and Ramanathan, V.: North American and Asian aerosols
547 over the eastern Pacific Ocean and their role in regulating cloud condensation nuclei, *J.*
548 *Geophys. Res. Atmos.*, doi:10.1029/2005JD006661, 2006.
- 549 Rosenfeld, D., Zhu, Y., Wang, M., Zheng, Y., Goren, T. and Yu, S.: Aerosol-driven droplet
550 concentrations dominate coverage and water of oceanic low-level clouds, *Science*,
551 doi:10.1126/science.aav0566, 2019.



- 552 Rosenfeld, D., Wang, H., and Rasch, P. J.: The roles of cloud drop effective radius and LWP in
553 determining rain properties in marine stratocumulus, *Geophys. Res. Lett.*, 39, L13801,
554 doi:10.1029/2012GL052028, 2012.
- 555 Seinfeld, J. H., Bretherton, C., Carslaw, K. S., Coe, H., DeMott, P. J., Dunlea, E. J., Feingold, G.,
556 Ghan, S., Guenther, A. B., Kahn, R., Kraucunas, I., Kreidenweis, S. M., Molina, M. J., Nenes,
557 A., Penner, J. E., Prather, K. A., Ramanathan, V., Ramaswamy, V., Rasch, P. J., Ravishankara,
558 A. R., Rosenfeld, D., Stephens, G. and Wood, R.: Improving our fundamental understanding
559 of the role of aerosol-cloud interactions in the climate system, *Proc. Natl. Acad. Sci. U. S. A.*,
560 doi:10.1073/pnas.1514043113, 2016.
- 561 Stein, A. F., Draxler, R. R., Rolph, G. D., Stunder, B. J. B., Cohen, M. D. and Ngan, F.: Noaa's
562 hysplit atmospheric transport and dispersion modeling system, *Bull. Am. Meteorol. Soc.*,
563 doi:10.1175/BAMS-D-14-00110.1, 2015.
- 564 Toll, V., Christensen, M., Quaas, J. and Bellouin, N.: Weak average liquid-cloud-water response
565 to anthropogenic aerosols, *Nature*, doi:10.1038/s41586-019-1423-9, 2019.
- 566 Twomey, S. and Twomey, S.: The Influence of Pollution on the Shortwave Albedo of Clouds, *J.*
567 *Atmos. Sci.*, doi:10.1175/1520-0469(1977)034<1149:TIOPOT>2.0.CO;2, 1977.
- 568 Ulbrich, C. W.: Natural variations in the analytical form of the raindrop size distribution., *J. Clim.*
569 *Appl. Meteorol.*, doi:10.1175/1520-0450(1983)022<1764:NVITAF>2.0.CO;2, 1983.
- 570 Wang, H. and Feingold, G.: Modeling mesoscale cellular structures and drizzle in marine
571 stratocumulus. Part I: Impact of drizzle on the formation and evolution of open cells, *J. Atmos.*
572 *Sci.*, doi:10.1175/2009JAS3022.1, 2009.
- 573 Wang, H., Rasch, P. J., Easter, R. C., Singh, B., Zhang, R., Ma, P.-L., Qian, Y., Ghan, S. J., and
574 Beagley, N. Using an explicit emission tagging method in global modeling of source-receptor
575 relationships for black carbon in the Arctic: Variations, sources, and transport pathways. *J.*
576 *Geophys. Res.*, 119, 12888–12909, 2014.
- 577 Wang, J., Wood, R., Jensen, M., Azevedo, E., Bretherton, C., Chand, D., Chiu, C., Dong, X., Fast,
578 J., Gettelman, A., Ghan, S., Giangrande, S., Gilles, M., Jefferson, A., Kollias, P., Kuang, C.,
579 Laskin, A., Lewis, E., Liu, X., Liu, Y., Luke, E., McComiskey, A., Mei, F., Miller, M.,
580 Sedlacek, A., Shaw, R.: Aerosol and Cloud Experiments in Eastern North Atlantic (ACE-
581 ENA) Field Campaign Report, DOE ARM Climate Research Facility, DOE/SC-ARM-19-



- 582 012, available at <https://www.arm.gov/publications/programdocs/doe-sc-arm-19-012.pdf>,
583 2019.
- 584 Wang, Y., Fan, J., Zhang, R., Leung, L. R. and Franklin, C.: Improving bulk microphysics
585 parameterizations in simulations of aerosol effects, *J. Geophys. Res. Atmos.*,
586 doi:10.1002/jgrd.50432, 2013.
- 587 Wang, Y., Wang, M., Zhang, R., Ghan, S. J., Lin, Y., Hu, J., Pan, B., Levy, M., Jiang, J. H. and
588 Molina, M. J.: Assessing the effects of anthropogenic aerosols on Pacific storm track using a
589 multiscale global climate model, *Proc. Natl. Acad. Sci. U. S. A.*,
590 doi:10.1073/pnas.1403364111, 2014.
- 591 Wang, Y., Vogel, J. M., Lin, Y., Pan, B., Hu, J., Liu, Y., Dong, X., Jiang, J. H., Yung, Y. L. and
592 Zhang, R.: Aerosol microphysical and radiative effects on continental cloud ensembles, *Adv.*
593 *Atmos. Sci.*, doi:10.1007/s00376-017-7091-5, 2018.
- 594 Weinzierl, B., Ansmann, A., Prospero, J. M., Althausen, D., Benker, N., Chouza, F., Dollner, M.,
595 Farrell, D., Fomba, W. K., Freudenthaler, V., Gasteiger, J., Groß, S., Haarig, M., Heinold, B.,
596 Kandler, K., Kristensen, T. B., Mayol-Bracero, O. L., Müller, T., Reitebuch, O., Sauer, D.,
597 Schäfler, A., Schepanski, K., Spanu, A., Tegen, I., Toledano, C. and Walser, A.: The Saharan
598 aerosol long-range transport and aerosol-cloud-interaction experiment: Overview and
599 selected highlights, *Bull. Am. Meteorol. Soc.*, doi:10.1175/BAMS-D-15-00142.1, 2017.
- 600 Wood, R., Wyant, M., Bretherton, C. S., Rémillard, J., Kollias, P., Fletcher, J., Stemmler, J., De
601 Szoeke, S., Yuter, S., Miller, M., Mechem, D., Tselioudis, G., Chiu, J. C., Mann, J. A. L.,
602 O'Connor, E. J., Hogan, R. J., Dong, X., Miller, M., Ghate, V., Jefferson, A., Min, Q., Minnis,
603 P., Palikonda, R., Albrecht, B., Luke, E., Hannay, C. and Lin, Y.: Clouds, aerosols, and
604 precipitation in the marine boundary layer: An arm mobile facility deployment, *Bull. Am.*
605 *Meteorol. Soc.*, doi:10.1175/BAMS-D-13-00180.1, 2015.
- 606 Wu, P., Dong, X., Xi, B., Tian, J. and Ward, D. M.: Profiles of MBL cloud and drizzle
607 microphysical properties retrieved from ground-based observations and validated by aircraft
608 in-situ measurements over the Azores, *J. Geophys. Res. Atmos.*, doi:10.1029/2019jd032205,
609 2020.
- 610 Yamaguchi, T., Feingold, G. and Kazil, J.: Aerosol-Cloud Interactions in Trade Wind Cumulus
611 Clouds and the Role of Vertical Wind Shear, *J. Geophys. Res. Atmos.*,
612 doi:10.1029/2019JD031073, 2019.



613 Zhao, B., Wang, Y., Gu, Y., Liou, K. N., Jiang, J. H., Fan, J., Liu, X., Huang, L. and Yung, Y. L.:
614 Ice nucleation by aerosols from anthropogenic pollution, *Nat. Geosci.*, doi:10.1038/s41561-
615 019-0389-4, 2019.

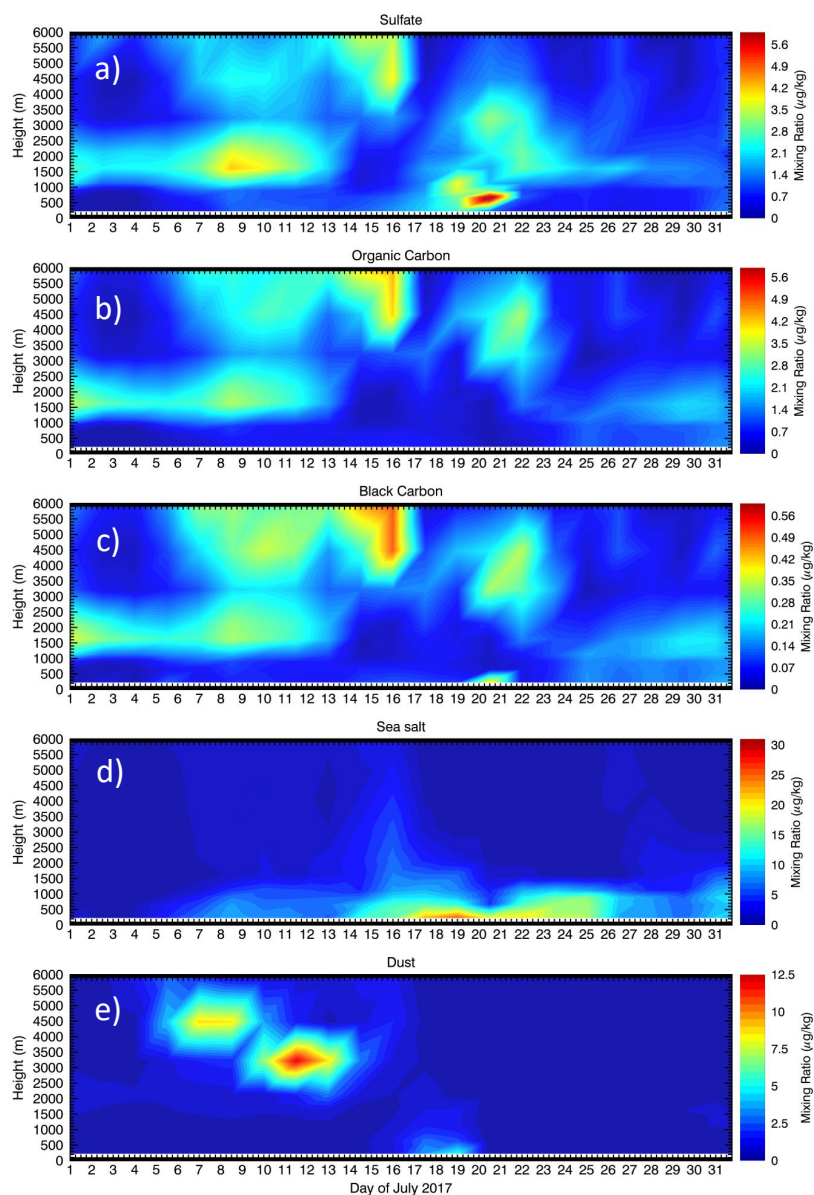
616 Zheng, X., Xi, B., Dong, X., Logan, T., Wang, Y. and Wu, P.: Investigation of aerosol-cloud
617 interactions under different absorptive aerosol regimes using Atmospheric Radiation
618 Measurement (ARM) southern Great Plains (SGP) ground-based measurements, *Atmos.*
619 *Chem. Phys.*, doi:10.5194/acp-20-3483-2020, 2020.

620

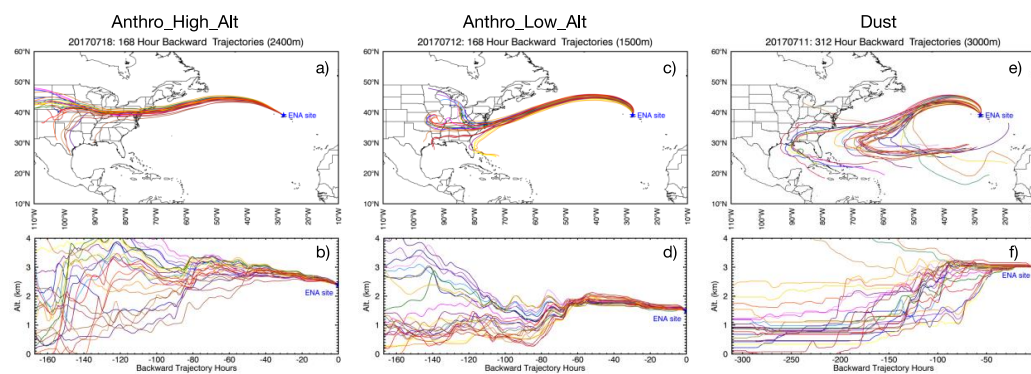
621

622

623 **Figures**



624
625 **Figure 1.** Temporal evolutions of vertical distributions for five types of aerosols as shown in a)
626 sulfate, b) organic carbon, c) black carbon, d) sea salt, and e) dust during July 2017 over the Azores
627 based on the ECMWF-CAMS aerosol reanalysis product.
628



629

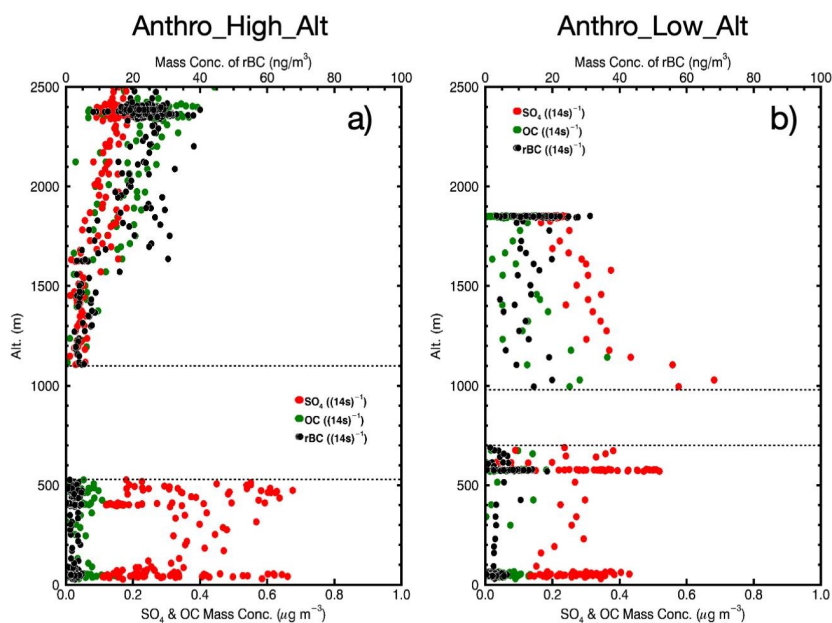
630 **Figure 2.** Back-trajectory analyses of air mass history starting from the ENA site for the three

631 selected cases using the NOAA HYSPLIT Trajectory Model. Anthropogenic aerosols dominated

632 plume with high altitude (Anthro_High_Alt) and low altitude (Anthro_High_Alt), dust plume

633 (Dust).

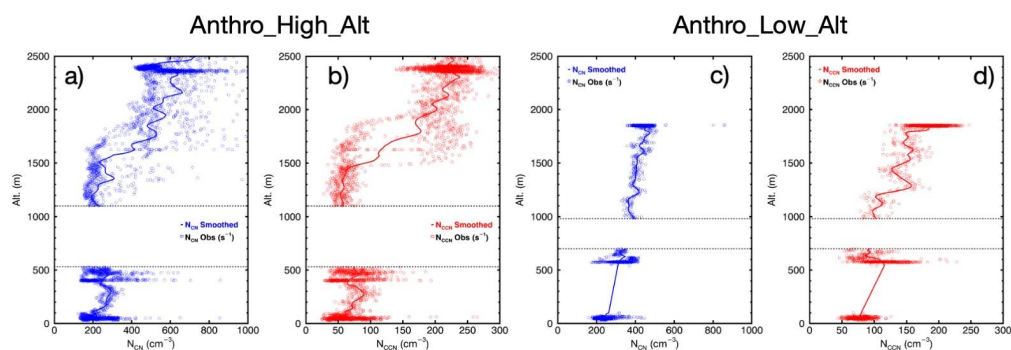
634



635

636 **Figure 3.** Airborne measured vertical profiles of sulfate (SO_4 , red dots), organic carbon (OC, green
637 dots), and refractory BC (rBC, black dots) mass mixing ratios averaged over multiple flights in
638 two characteristic cases: (a) high-altitude aerosol plume on 18 July and (b) low-altitude aerosol
639 plume on 12 July, 2017. The highly uncertain and noisy aerosol observations due to cloud
640 contamination are not shown (between two dash lines), so the blank regions approximately denote
641 cloud layer.

642



643

644

Figure 4. Airborne measured profiles of condensation nuclei (N_{CN}) and cloud condensation nuclei

645

(N_{CCN}) averaged over multiple flights in two cases with high- and low-altitude aerosol plumes.

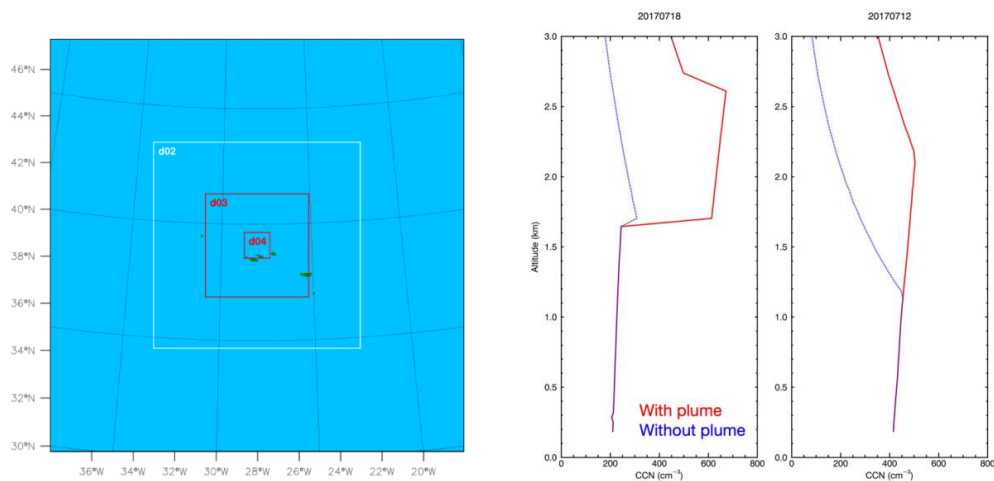
646

The highly uncertain and noisy aerosol observations due to cloud contamination are not shown

647

(between two dash lines), so the blank regions approximately denote cloud layer.

648

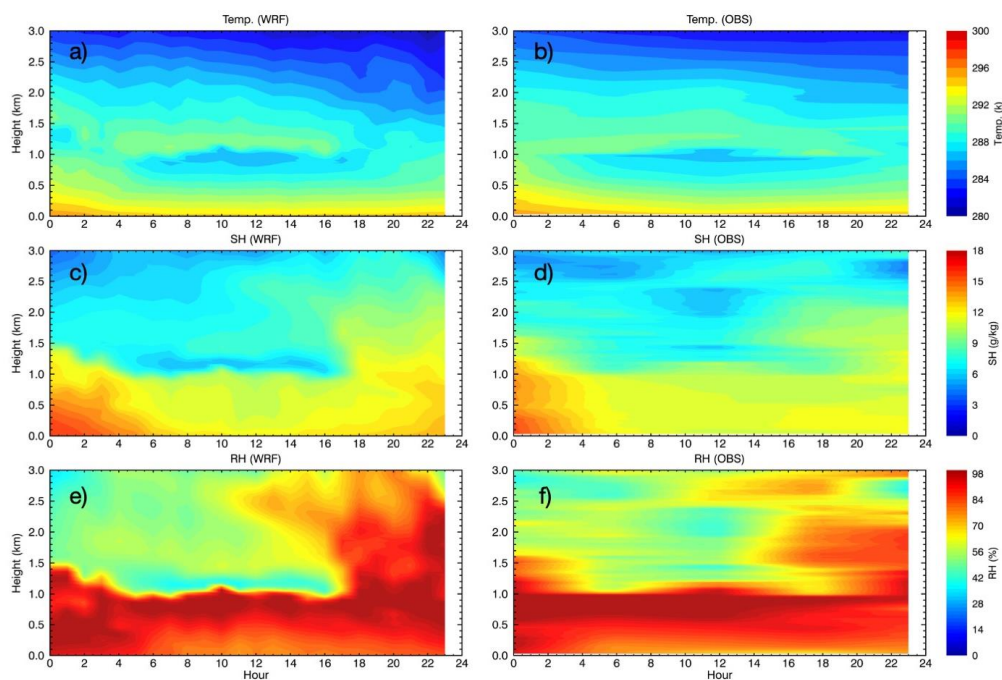


649

650 **Figure 5.** WRF domain map and aerosol concentration profiles used in the model as initial and

651 boundary conditions for the sensitivity runs of the two cases.

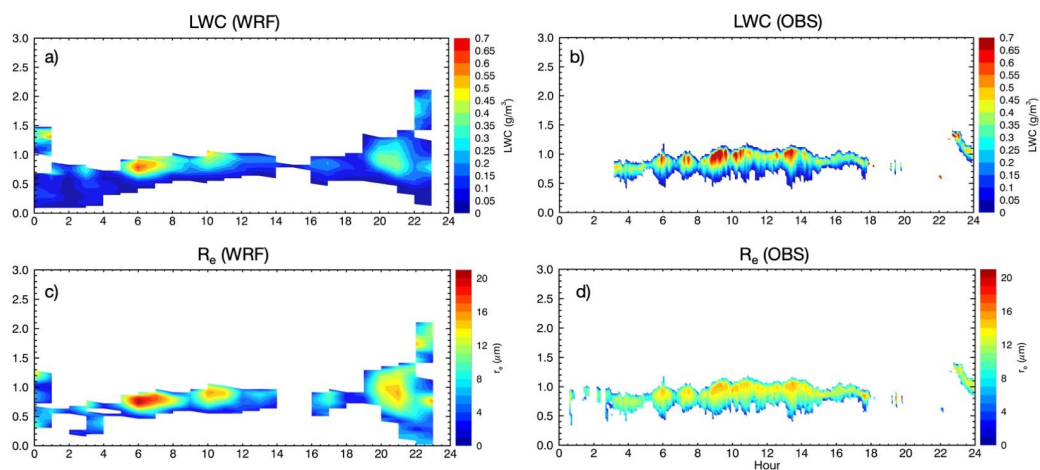
652



653

654 **Figure 6.** WRF simulated (left panels) and merged sounding measured (right panels)
655 spatiotemporal evolutions of air temperature (the first row), specific humidity (the second row),
656 and relative humidity (the third row) for the high-altitude plume case.

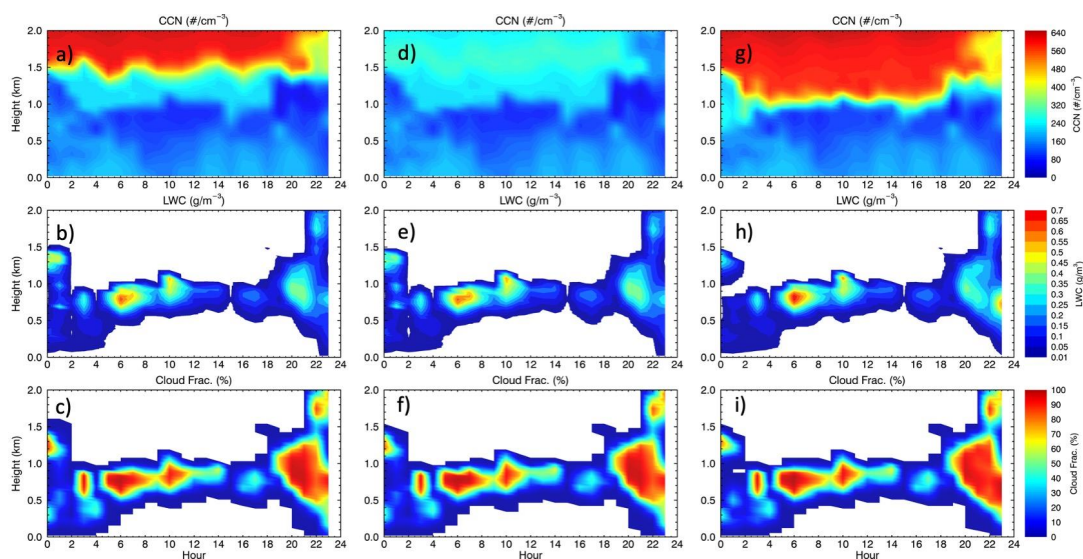
657



658

659 **Figure 7.** WRF simulated (top panels) and cloud radar retrieved (bottom panels) spatiotemporal
660 evolution of liquid water content (the left column) and droplet effective radius (the right column)
661 for the high-altitude plume case.

662



663

664

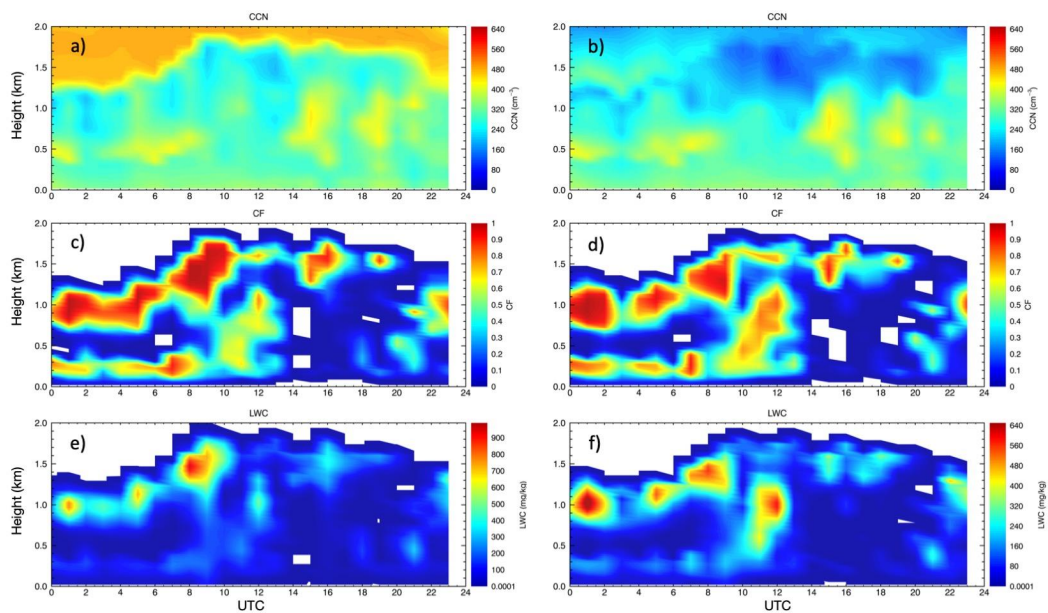
665

666

667

668

Figure 8. WRF simulated CCN concentration, liquid water content (LWC), and cloud fraction for the high-altitude plume case (averaged over 20×20 grid points): a-c) with the observed aerosol plume due to long-range transport (above 1.5 km), d-f) with the aerosol plume removed, and g-i) with the aerosol plume moved downward to 1.1 km.

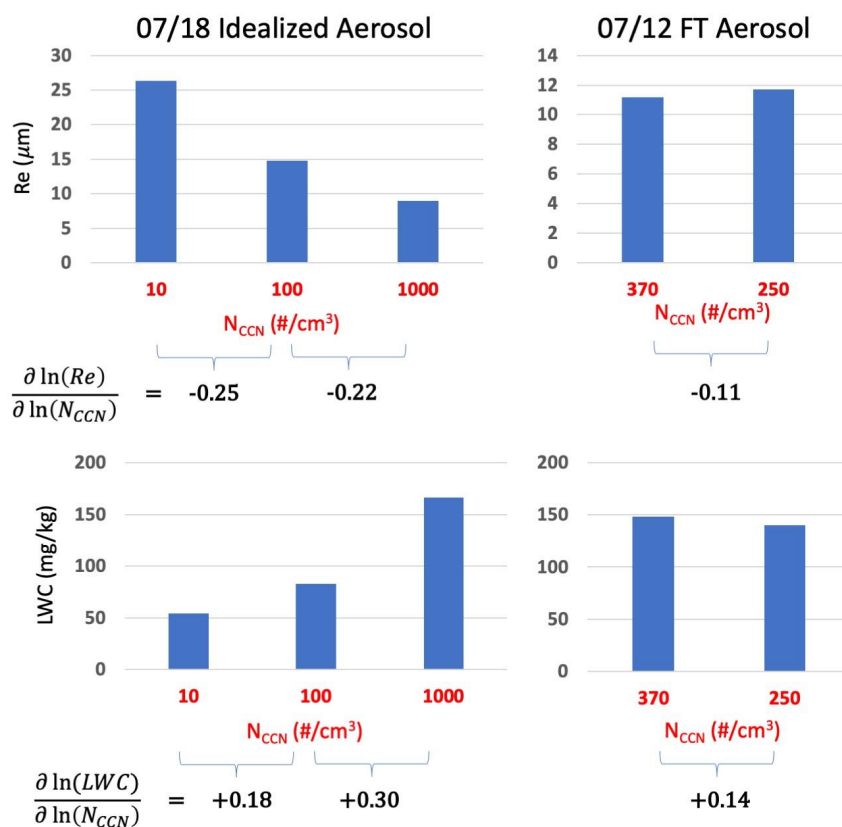


669

670 **Figure 9.** WRF simulated CCN concentration, liquid water content (LWC), and cloud fraction for

671 the low-altitude plume case.

672



673

674 **Figure 10.** Model predicted cloud susceptibilities for the idealized CCN variations in the MBL
 675 for the July 18 case and the influence of CCN variations in the free troposphere (FT) for the July
 676 12 case. The cloud properties are averaged over all cloud points in the innermost domain. N_{CCN}
 677 values are obtained from the initial CCN profiles and averaged over between 0.5-3 km.

678



679 **Table 1.** Characteristics of condensation nuclei concentration (CN) and cloud vertical profiles for
 680 all eight cases during the summer phase of the DOE ACE-ENA field campaign.

Date of Flight	Cloud Type	Above-Cloud Aerosol Changes with Height	Above-cloud N_{CN}^* (# cm^{-3})	Below-cloud N_{CN}^* (# cm^{-3})	Cloud Top Height Variation** (m)	Critical Altitude*** (m)
20170628	Thin Stratus	Increase	471	353	670 - 1060	N/A
20170630	Thin Stratus	Increase	456	391	820 - 1270	N/A
20170706	StCu.	Keep constant	354	272	1210 - 1720	1820
20170707	Stratus	Decrease	266	247	1540 - 1960	N/A
20170712	StCu.	Increase	464	331	760 - 1360	N/A
20170715	StCu.	Increase	237	205	1120 - 1750	N/A
20170718	StCu.	Increase	185	290	880 - 1300	1674
20170720	StCu.	Decrease	224	311	970 - 1660	N/A

681 * Average within 200 m of above (below) cloud top (base)

682 ** For continuous cloud layer

683 *** Critical altitude is defined as the height at which above-cloud N_{CN} is equal to the below-

684 cloud N_{CN} .